Ion-Hong Chao
Mechanical and Aerospace Engineering Department,
University of California, Los Angeles,
Los Angeles, CA 90024
e-mail: dennischao@ucla.edu

Liang Pan
Mechanical Engineering Department,
Purdue University,
West Lafayette, IN 47907
e-mail: liangpan@purdue.edu

Cheng Sun
Mechanical Engineering Department,
Northwestern University,
Evanston, IL 60208
e-mail: c-sun@northwestern.edu

Xiang Zhang
Mechanical Engineering Department,
University of California, Berkeley,
Berkeley, CA 94709
e-mail: xzhang@me.berkeley.edu

Adrienne S. Lavine
Mechanical and Aerospace Engineering Department,
University of California, Los Angeles,
Los Angeles, CA 90024
e-mail: lavine@seas.ucla.edu

A Coupled Electromagnetic and Thermal Model for Picosecond and Nanometer Scale Plasmonic Lithography Process

Plasmonic lithography may become a mainstream nanofabrication technique in the future. Experimental results show that feature size with 22 nm resolution can be achieved by plasmonic lithography. In the experiment, a plasmonic lens (PL) is used to focus the laser energy with resolution much higher than the diffraction limit and features are created in the thermally sensitive phase-change material (PCM) layer. The energy transport mechanisms are still not fully understood in the lithography process. In order to predict the lithography resolution and explore the energy transport mechanisms involved in the process, customized electromagnetic wave (EMW) and heat transfer (HT) models were developed in COMSOL. *Parametric studies on both operating parameters and material properties were performed to optimize the lithography process. The parametric studies show that the lithography process can be improved by either reducing the thickness of the phase-change material layer or using a material with smaller real refractive index for that layer.* [DOI: 10.1115/1.4027589]

Introduction

Plasmonic lithography may become the next generation nanofabrication technique, mainly because of its ability to overcome the diffraction limit on resolution. During conventional photolithography fabrication, the desired pattern is created using a set of photomasks, which are very expensive and time-consuming to make. Moreover, resolution in photolithography is limited by the diffraction limit [1]. Other nanolithography techniques, such as electron-beam [2], focused ion-beam [3], etc, can generate high-resolution patterns without using a mask, but their production rates under the serial patterning process are far from the industrial requirement. Plasmonic lithography is capable of generating high resolution patterns at high speed with parallel processing to meet industrial needs [4].

Despite the promise of plasmonic lithography, the energy transport mechanisms that occur during the process are not well understood. In this paper, a coupled electromagnetic and thermal numerical model is presented that explores mechanisms for optimizing the plasmonic lithography fabrication process.

Three important elements of the plasmonic lithography process are: (1) a coherent laser, (2) a plasmonic lens structure on a metal thin film; this is a concentric grating with a specially designed small aperture, and (3) a substrate on which patterns are generated due to a phase change. The coherent laser pulse excites surface plasmons on the metal thin film, which are focused by the plasmonic lens structure. The substrate is positioned a few nanometers beneath the plasmonic lens, allowing near-field energy to be transported across the gap and absorbed in the PCM. When the temperature of the PCM exceeds a threshold, it experiences a phase change to form the lithography pattern. The size of the phase-change region determines the resolution of the process. Patterns with 22 nm half-pitch resolution have been demonstrated experimentally [5]. In order to predict the lithography resolution, a customized numerical model was developed in COMSOL to solve the coupled electromagnetic and thermal problem. Maxwell's equations were used to model focusing of the laser energy by the plasmonic lens structure and the resulting energy absorption in the PCM. Then, the transient heat conduction equation was solved to obtain the temperature profile in the PCM and thereby determine the size of the phase-change region. Moreover, since the properties of the PCM are not well known, refractive index and thermal conductivity were measured by ellipsometry [6] and the three-omega method [7], respectively, and used as property inputs.

The numerical model is used to examine the effect of performance when varying different operating parameters, such as laser power, laser pulse duration, laser spot size, the nanometer scale gap size, the thickness of the PCM layer, etc. The effect of the PCM's optical and thermal properties is also examined to account for experimental uncertainty in these values and to consider the possibility of developing improved materials for this process. The model is shown to have value in optimizing the process of plasmonic lithography.

Experimental System and Principles of Plasmonic Lithography

An experimental system for plasmonic lithography basically consists of a UV laser source (355 nm wavelength) with optical setup, a plasmonic flying head with fabricated PL, and a rotating disk with a multilayer structure. A simplified diagram of the experimental system is shown in Fig. 1.

An optical modulator is used to convert the continuous UV laser output into a series of laser pulses. The typical pulse

Contributed by the Manufacturing Engineering Division of ASME for publication in the JOURNAL OF MICRO- AND NANO-MANUFACTURING. Manuscript received March 1, 2014; final manuscript received April 30, 2014; published online July 8, 2014. Editor: Jian Cao.

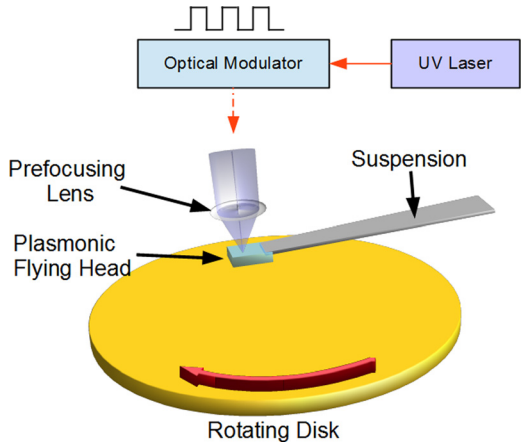

Fig. 1 Diagram of plasmonic lithography. A UV laser is focused through an optical (prefocusing) lens and a plasmonic lens to create a nanoscale pattern on the phase-change material on the rotating disk.

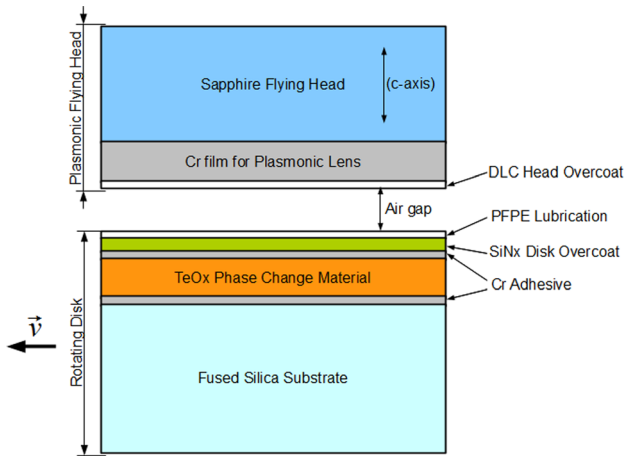

Fig. 2 Layer structure of plasmonic lithography. A plasmonic lens is fabricated on the chromium layer underneath the sapphire flying head. When laser energy is focused by the plasmonic lens, the phase-change patterns are created on the TeO_x-based phase-change material.

frequency is 160 MHz, and the typical duration of each pulse is 12 ps full width at half maximum (FWHM). The pulsed laser is prefocused by the optical lens to the micrometer scale before reaching the flying head. A plasmonic lens is fabricated on the downward-facing surface of the sapphire flying head, which allows the pulsed laser energy to be further focused down to the nanometer scale. The intensely focused energy causes a phase change in the material on the rotating disk. The flying head is supported by the suspension arm and flies over the rotating disk to create the desired pattern on the phase-change material. Because of the near-field nature of the radiation transmitted through the plasmonic lens, the bottom surface of the plasmonic flying head and the top surface of the rotating disk must be maintained within a few nanometers gap distance. The disk is rotating at a linear speed of about 7 m/s. Since the dimension of the flying head is in the millimeter scale, it is challenging to maintain the nanoscale gap without destructive contact during the lithography process. The solution to this challenge is presented in Ref. [4]. Instead of using a rotating disk, one possible approach is to put the substrate on a linear piezo stage but a rotating disk provides continuous and constant motion without acceleration and deceleration, which is important for increasing the patterning throughput.

The layer structure of the plasmonic lithography process is shown in Fig. 2. From top to bottom, the plasmonic flying head is made of an approximately 0.5 mm thick sapphire, a 60 nm chromium layer on which the PL is fabricated, and an approximately 5 nm diamond-like-carbon (DLC) layer for PL protection during the lithography process. Between the plasmonic flying head and rotating disk is the nanoscale air gap or so-called air bearing surface. The typical experimental air gap distance is about 2 nm.

The rotating disk is mainly prepared by sputtering the desired layers on a fused silica disk substrate. The layers on the fused silica disk are deposited by RF magnetron sputtering. The 5 nm thick chromium layer is first deposited as an adhesive layer. Next, the TeO_x-based PCM is deposited [8]. The typical thickness of PCM is about 20–30 nm. The sputtering target of PCM is a solid mixture of TeO_2, Te, and Pd with weight percentages of 80%, 10%, and 10%, respectively. Since the sputtering chamber contains argon and oxygen, the percentages of constituents in the fabricated PCM are expected to be different from that of the sputtering target. An additional chromium adhesive layer with thickness about 2 nm is deposited on top of the PCM layer. Then a silicon nitride (SiN_x) layer with thickness about 4 nm is deposited. During the sputtering process, the series of layers is deposited without breaking the vacuum inside the chamber to ensure the quality of PMC layer and avoid oxidation. After the sputtering process, about 1 nm thick perfluoropolyether (PFPE) lubricant layer is coated on the top surface of the rotating disk. The combination of PFPE lubrication and SiN_x disk overcoat can protect the PCM layer from damage during the lithography process.

Some amount of laser energy is lost from the UV laser source before reaching the PL. As shown in Fig. 1, a prefocusing objective lens is placed between the exit of the optical modulator and the plasmonic flying head to focus the laser energy on the PL. In order to estimate the amount of laser energy loss, values of laser energy are measured at the outlet of the UV laser source and the outlet of the prefocusing lens. Then the transmissivity at the top surface of the sapphire flying head can be calculated from Fresnel equations by using refractive indices of air and sapphire. As a result, it is estimated that about 50% of the energy from the UV laser source arrives at the PL, and the remaining 50% of energy is lost within the optical setup.

The prefocusing lens is used to focus the laser energy on the PL with the spot diameter in the micrometer scale. The refractive index of sapphire along the *c*-axis is different from the other directions. The focused laser pulse from the prefocusing lens needs to go through the sapphire flying head before arriving at the PL. The anisotropic optical property of sapphire increases the difficulty to predict the exact laser spot diameter right before reaching the PL. Instead of calculating the exact size and profile of laser spot by handling the anisotropy, the spot diameter is estimated from the experimental results. The estimated spot diameter is on the order of one micrometer, and will be discussed further.

The geometry of the PL is shown in Fig. 3. The PL is fabricated on the chromium film underneath the flying head, and includes concentric ring grooves and center aperture. The PL is designed to effectively focus the laser energy with resolution of tens of nanometers. When the electric field is oriented in the direction specified in Fig. 3, the focused surface plasmons generate a strong electric field across the narrow gap in the dog-bone shaped center aperture. That small region of strong electric field delivers energy to the rotating disk at high resolution.

A significant portion of the energy from the strong electric field at the center aperture converts to heat inside the PCM and chromium adhesive layers, which have relatively larger absorption indices. When temperature increases to a certain threshold, phase change starts inside the PCM. At this point, the desired patterns are created in the phase-changed region inside the PCM layer. A subsequent development process removes the phase-changed region to create a permanent pattern on the PCM layer [9]. The size and depth of the developed patterns have been measured by atomic force microscopy, which are about 20 nm and 1 nm,

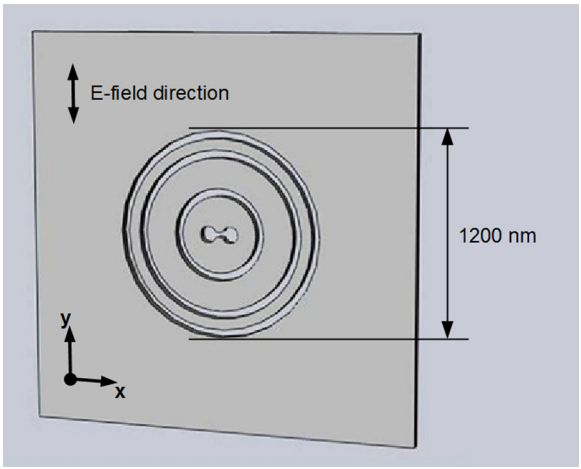

Fig. 3 Plasmonic lens geometry. A single plasmonic lens includes concentric ring grooves and center aperture. The rings help to focus the UV laser excited surface plasmons on the center aperture. When the electric field of the incident laser is oriented in the specific direction, strong electric field is generated across the narrow gap in the dog-bone-shaped center aperture to highly focus the laser energy.

respectively, for similar experimental conditions [5]. A microscope image of the plasmonic lithography pattern array is shown in Fig. 4. It can be seen from this figure that the pattern size increases (seen as a brighter pattern) as the laser power increases. This characteristic will be compared with model results in the Results and Parametric Study section.

Numerical Models

In order to simulate the plasmonic lithography process, both EMW model and HT model are used.

Assumptions. Different assumptions have been made for the electromagnetic wave model and heat transfer model in order to simplify and increase their efficiency.

The laser pulse duration is on the order of 10^{-11} s, and the electromagnetic wave period of the UV laser is on the order of 10^{-13} s, so the UV laser may be modeled as a harmonic electromagnetic wave with time-dependent electric field magnitude. Thus, the phasor form of Maxwell's equation is used instead of the full transient form. The optical properties used in the electromagnetic wave model are assumed to be constants, with the values of properties evaluated at the frequency of the UV laser. In this lithography experiment, some materials are physically isotropic, and some are isotropic because they were created by sputtering. The sapphire flying head has about 0.5% anisotropy between ordinary ray and extraordinary ray (c-axis); it is assumed that this small anisotropy would only slightly affect the results, so the flying head material is also assumed to be isotropic. Moreover, all the materials are nonmagnetic. By assuming that the flying head material has isotropic and constant optical properties, the laser beam is assumed to be a Gaussian beam with focal point at the center of the PL. In the EMW model, the DLC head overcoat and PFPE lubrication are excluded because they are much thinner than the PL chromium layer. The thin layers on the rotating disk substrate are deposited by sputtering. As a result, the interfaces between layers are not very precise, but they are assumed to be precisely flat in the numerical models. From the drawing of the PL in Fig. 3, the geometry of the PL is symmetric about the x-axis and y-axis, so the EMW model only solves for one-quarter of the PL.

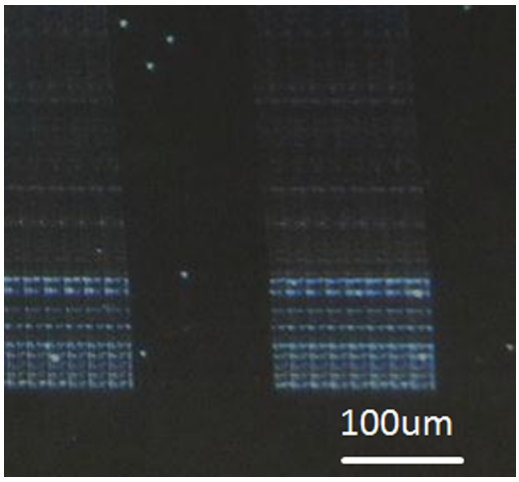

Fig. 4 Microscope image of plasmonic lithography pattern array. From top to bottom, pattern size increases as the laser power increases.

The output from the EMW model provides the spatial variation of volumetric heat generation within the rotating disk layers, which serves as an input to the HT model. The HT model includes only the rotating disk, not the flying head. The top PFPE lubrication is also excluded from the HT model because of its small thickness. The disk substrate is fused silica which is amorphous and isotropic. The layers on top of the disk substrate, which are deposited by sputtering, are highly disordered and isotropic. Therefore, thermal properties in the HT model can be assumed as isotropic [10]. Moreover, properties in the HT model are also assumed as constants. In crystalline material, thermal energy is carried by phonons, which are quanta of lattice vibrations. However, inside the disordered material, phonon scattering is very likely to be significant [11]; heat transfer can therefore be treated as a diffusive process, and the parabolic heat transfer equation is used in the HT model. Within the pulse duration, the disk moves a distance on the order of 0.1 nm, and the feature size from the plasmonic lithography is on the order of 10 nm. Therefore, the disk can be assumed stationary relative to the PL.

The top surface of the rotating disk is modeled as thermally insulated, based on two assumptions. First, inside the air gap between the flying head and rotating disk is rarefied gas, so convection is assumed negligible. Second, an estimate shows that conventional radiation heat transfer is also negligible. Radiative energy loss from a 22 nm-radius circular spot with 573 K phase-change temperature to the 298 K surrounding within 12 ps is about 1.0×10^{-22} J by assuming black body radiation. The energy required to heat the PCM cylinder from 298 K to 573 K with a typical 22 nm radius and 6 nm height is 5.8×10^{-15} J. Since the radiative energy loss is many orders of magnitude smaller than the energy required for heating, it is reasonable to neglect radiation heat transfer. However, it should be noted that this analysis does not account for near-field radiation and the effect of the elevated temperature of the flying head; this is an area for future research.

Flow Chart of Numerical Models. The interrelationship between the EMW and HT models is shown in Fig. 5. In this figure, the experimental parameters are labeled in green and the calculated variables and material properties are labeled in blue. The governing equations for both EMW and HT models are in purple and the results from the models are in yellow. The desired lithography feature size is in orange in the lower right corner. The arrows show the input and output variables and calculation sequence.

The overall process of simulation is to use the EMW model to determine the resistive heating caused by the laser illumination, then use the resistive heating as the heat source in the HT model to solve for the time-dependent temperature distribution. The desired lithography feature size is determined by the size of the

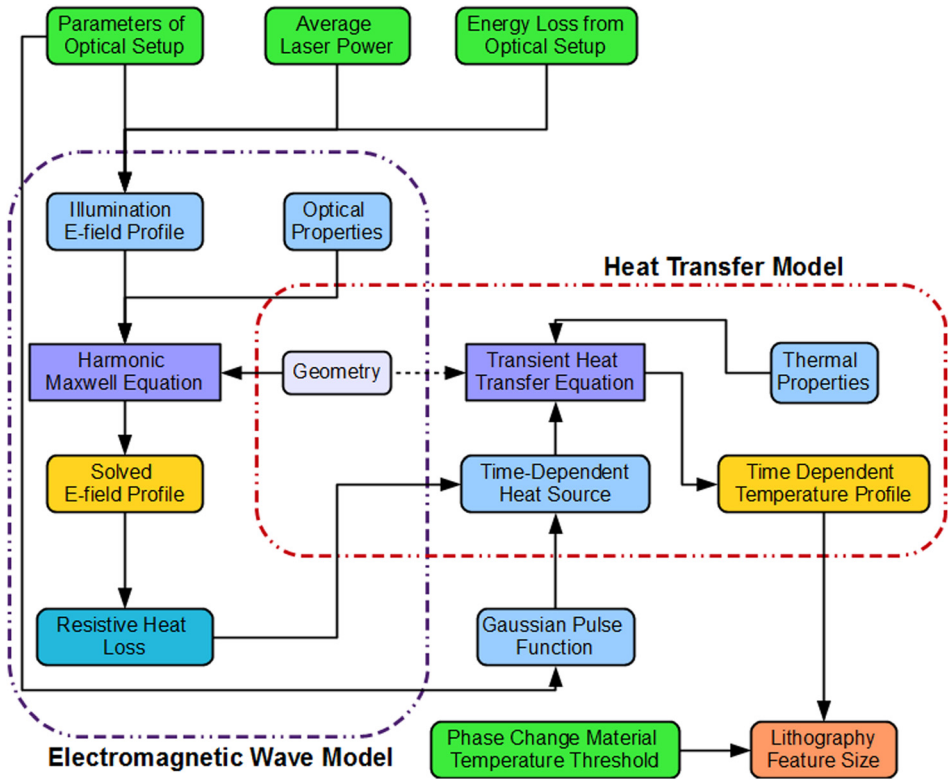

Fig. 5 Inputs and outputs of electromagnetic wave and heat transfer models

phase-change region in the PCM, which can be evaluated from the temperature distribution and the threshold temperature for phase change. As an input for the EMW model, the E-field profile of the illumination laser is obtained from knowledge of the average laser power, laser pulse duration, focus spot size, and energy losses in the optical setup. Resistive heat loss can be calculated from the resolved electric field and refractive indices of materials. The time dependency of laser pulse intensity is represented by a Gaussian distribution. The resistive heating from the EMW model and the Gaussian function provide both the magnitude and time dependency for the time-dependent heat source, which is an input for the HT model.

Electromagnetic Wave Model. Since the electromagnetic wave period of the UV laser (corresponding to 355 nm wavelength) is much smaller than the laser pulse duration, the governing equation used in the EMW model is

$$\nabla \times \mu_r^{-1}(\nabla \times \mathbf{E}) - k_0^2\left(\varepsilon_r - \frac{j\sigma}{\omega\varepsilon_0}\right)\mathbf{E} = 0 \tag{1}$$

which is the phasor form of Maxwell's equation, instead of the full transient form. In Eq. (1), $\mathbf{E}$ is the electric field phasor, ε_0 and ε_r are vacuum permittivity and relative permittivity, μ_r is the relative permeability (equal to one for nonmagnetic materials), σ and ω are electric conductivity and angular frequency, respectively, k_0 is the magnitude of the vacuum wave vector for the UV laser, and j is the imaginary unit. The complex refractive index is defined as

$$n_c^2 = \mu_r\left(\varepsilon_r - \frac{j\sigma}{\omega\varepsilon_0}\right) \tag{2}$$

Therefore, with the constant properties assumption, Eq. (1) can be written as

$$\nabla \times (\nabla \times \mathbf{E}) - n_c^2 k_0^2 \mathbf{E} = 0 \tag{3}$$

Thus, the required optical properties in the EMW model are just the complex refractive indices of materials.

Geometries and domains for the EMW model are shown in Fig. 6, which includes the sapphire flying head, PL, air gap, and the layers on the rotating disk substrate; the figure also shows the corresponding materials. The z-axis is used as a center line for the PL. The boundary conditions of the EMW model are shown in Fig. 7. Since only one quarter of the PL is included in the numerical model due to symmetry, with the electric field of incident UV laser oriented in the y-axis direction, the xz-plane and yz-plane are set to be perfect electric conductor (PEC) and perfect magnetic conductor (PMC), respectively, to make the electric field perpendicular and parallel to the corresponding boundaries. The equations for PEC and PMC boundaries are

$$\hat{\mathbf{n}} \times \mathbf{E} = 0 \tag{4}$$

and

$$\hat{\mathbf{n}} \times \mathbf{H} = 0 \tag{5}$$

where $\mathbf{H}$ is the magnetic field phasor and $\hat{\mathbf{n}}$ is surface unit normal vector. The remaining four boundaries are set to be scattering boundaries with expression as

$$\hat{\mathbf{n}} \times (\nabla \times \mathbf{E}) - jk\hat{\mathbf{n}} \times (\mathbf{E} \times \hat{\mathbf{n}}) = -\hat{\mathbf{n}} \times (\mathbf{E_i} \times (jk(\hat{\mathbf{n}} - \mathbf{k_{dir}})))e^{-j\mathbf{k_{dir}}\cdot\mathbf{r}} \tag{6}$$

In the above equation, $\mathbf{E_i}$ is incident electric field phasor, k is magnitude of the wave vector, $\mathbf{k_{dir}}$ is directional wave vector, and $\mathbf{r}$ is position vector. A scattering boundary can be used to generate an electric field with the desired profile and also allows the incoming plane wave to pass through [12,13]. Therefore, a scattering boundary provides a good approximation for an open boundary in this EMW model. In order to simulate the UV illumination, a certain electric field profile, expressed as Eq. (A1) in Appendix A, is

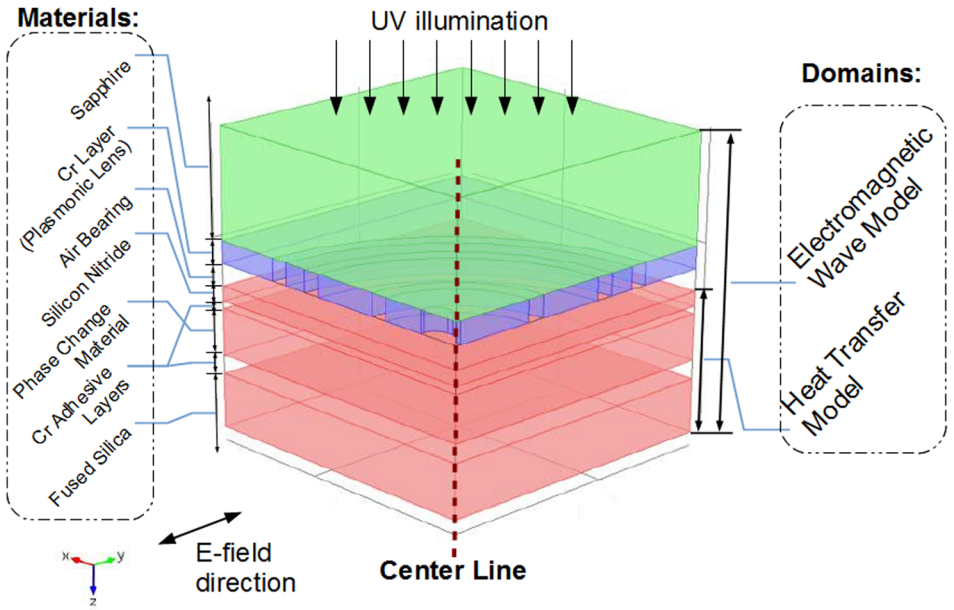

Fig. 6 Geometry, domains, and materials for electromagnetic wave and heat transfer models (not to scale)

used for the incident electric field profile at the top scattering boundary in Fig. 7. The incident electric field profiles for the other three scattering boundaries are set to be zero, since no electric field is generated on those boundaries.

The numerical software for the EMW model has been validated by comparison with analytical solutions for simple cases, such as a normal incident plane wave on a semi-infinite solid and a multilayer structure.

Heat Transfer Model. The governing equation used in the HT model is

$$\rho C_{\mathrm{p}} \frac{\partial T}{\partial t} = \nabla \cdot (k_{\mathrm{th}} \nabla T) + Q \tag{7}$$

which is the transient parabolic heat conduction equation. In the above equation, T is temperature, t is time, ρ is density, C_{p} is specific heat, k_{th} is thermal conductivity, and Q is volumetric heat source. Geometries and domains of the HT model can also be found in Fig. 6 but the HT model only includes the layers and substrate of the rotating disk. The plasmonic flying head and the air gap are excluded from the HT model. In the HT model, the change of temperature is driven by the time-dependent and space-dependent volumetric heat source.

All six boundaries for the HT model are thermally insulated, which is expressed as

$$-\hat{\mathbf{n}} \cdot (-k_{\mathrm{th}} \nabla T) = 0 \tag{8}$$

The HT model has been validated by comparison with the analytical solution for a uniform heat flux over a circular region on the surface of a semi-infinite solid.

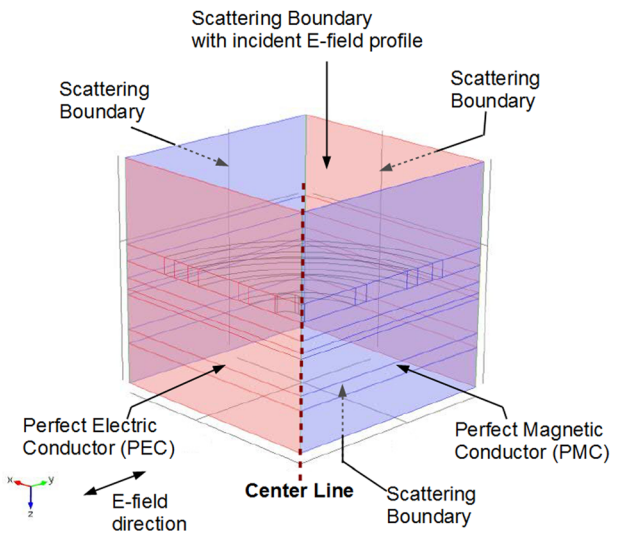

Fig. 7 Boundary conditions for electromagnetic wave model

Model Inputs. Besides the material properties, the electric field profile and time-dependent heat source need to be calculated as inputs for the EMW model and HT model.

The UV laser illumination is represented by the boundary electric field profile, which is a needed input to the EMW model. Given the known laser power, pulse duration, and FWHM focused laser spot diameter, the electric field distribution can be derived as shown in Appendix A, to yield the incident electric field profile for the top scattering boundary in Fig. 7.

Similarly, the time-dependent and space-dependent resistive heating is a needed input to the HT model. This can be related to the electric field solution from the EMW model, as shown in Appendix B, to give time-dependent heat source from the time-independent resistive heating.

Input parameters for both models can be categorized into either material properties or operating parameters. Material properties include real and imaginary part of refractive indices, densities, specific heats, and thermal conductivities. Material properties for both models are available in the literature except those for the PCM layer [14–17]. The complex refractive index of the PCM at 355 nm wavelength was measured by multi-angle ellipsometry and found to be $3.34 - j2.93$. The density and specific heat of PCM were estimated by the composite rule based on the constituent percentages of the PCM sputtering target. The estimated volumetric heat capacity, ρC_{p}, is 2.32×10^6 J/(m^3 K). The thermal conductivity of the PCM was measured by the differential 3ω method and found to be 1.12 W/(m·K) with uncertainty about

Table 1 Material properties and operating parameters in base case [14–17]

		Materials					
		Sapphire	Chromium	Air gap	Silicon nitride	PCM	Fused silica
Material Properties	Real refractive index	1.79	1.35	1	2.1	3.34	1.48
	Imag refractive index	0	3.2	0	0	2.93	0
	Thermal conductivity	—	93.9	—	8	1.12	1.38
	Density (kg/m^3)	—	7190	—	3200	6250	2200
	Heat capacity	—	449	—	1667	372	741
	Phase change temperature	—	—	—	—	573	—
Operating Parameters	Layer thickness (nm)	—	PL 60	2	4	25	—
			Top adhesive 2				
			Bottom adhesive 5				
	Focused spot diameter (μm)			1			
	Avg laser power when reaching PL (mW)			4.5			
	Laser pulse duration (ps)			12			
	Laser pulse frequency (MHz)			160			

25%. In the later discussion, the uncertainty of the PCM thermal conductivity is shown to have an insignificant effect on the lithography result.

Operating parameters include the PCM and other layer thicknesses, air gap distance, laser power, pulse duration, and focused laser spot size. All of the material properties and operating parameters are summarized in Table 1. Values in this table are used as the "base case" in the parametric study. Besides the focused laser spot size, all parameters are set to be equal to those in the typical experimental condition. The unknown focused laser spot size is estimated by comparing numerical and experimental results for a typical condition, as explained below.

Results and Parametric Study

The domain size, grid refinement, and time step size have been investigated in order to obtain high accuracy of the numerical solution. The domain size of the numerical model was shown to be large enough to eliminate any boundary effect in the numerical solution of the phase-change region. The grid and time step were refined until the numerical solution became independent of the grid and time step.

The time-dependent heat source for the HT model can be calculated based on the resistive heating and laser pulse duration (Eq. (B3) in Appendix B). The heat source distribution at the top surface of the PCM layer is shown in Fig. 8. In this figure, the time-dependent heat source is evaluated when the laser pulse reaches its peak value. The origin of this figure corresponds to the point below the center of the PL. By inspection, electromagnetic energy from the laser pulse is focused in a region within tens of nanometers right below the center of the PL, as desired.

The temperature distribution of the PCM after three standard deviations of time from the center mean time of the Gaussian laser pulse is shown in Fig. 9. The isotherm at the phase-change threshold temperature (573 K) is also plotted. The upper plot in this figure is the temperature distribution at the top surface of the PCM layer, which is parallel to the *xy*-plane. The lower plot is the temperature distribution at the *xz*-plane cross section of the PCM layer. For the lower plot, the *z*-axis starts at the top surface of the PCM layer to show the thermal penetration depth. The region enclosed by the 573 K isotherm has high enough temperature to cause phase change. Since phase change is an irreversible process, the determination of whether or not phase change occurs must be made based on the maximum temperature reached at a specific location. Since the maximum temperatures are not all reached at the same time, isotherms from each time step are overlapped together to determine the phase-change region; the 573 K isotherm at the end of the laser pulse in Fig. 9 is approximately, but not exactly, the same size as the phase-change region.

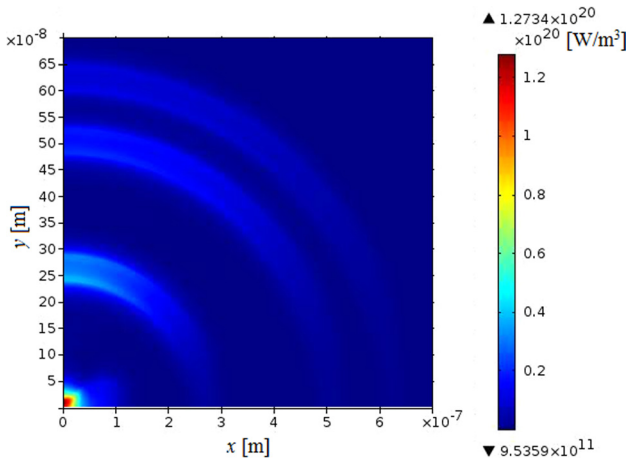

Fig. 8 Heat source distribution at the top surface of PCM layer. This heat source profile is captured when the laser pulse reaches its peak value. This figure shows the strong focusing effect of the PL.

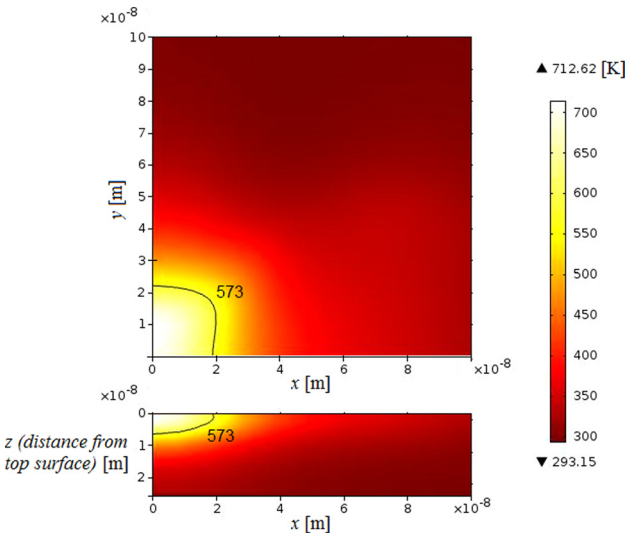

Fig. 9 Temperature distribution of PCM layer with isotherm at phase-change temperature. From top to bottom are the temperature distributions of PCM layer top surface (parallel to *xy*-plane) and PCM layer cross section (*xz*-plane) at the end of laser pulse.

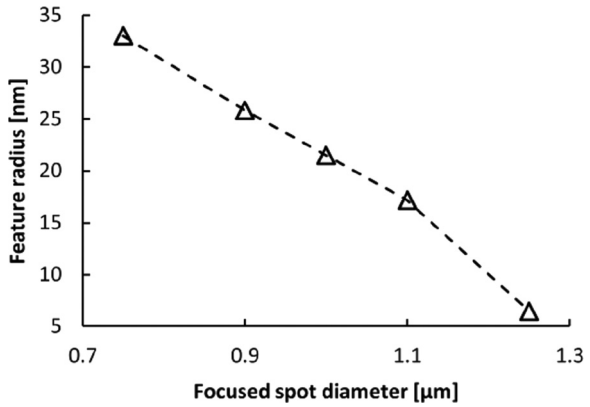

Fig. 10 Lithography feature radius as a function of laser focused spot diameter. Feature sizes are obtained by varying the objectively focused laser spot diameter with other numerical parameters unchanged.

Because the focused laser spot size before reaching the PL is unknown, different values of focused spot diameters are used to calculate the corresponding feature sizes, specifically the radius of the phase-change region at the top surface of the PCM layer. The calculated feature sizes are compared with the experimental result for the base case condition to estimate the reasonable focused spot size in the experiment. The calculated feature radius as a function of focused laser spot size is plotted in Fig. 10. Since feature size from the experiments is 22 nm [5], the typical focused laser spot diameter is expected to be about 1 μm based on this figure. The estimated spot diameter is the same order of magnitude as expected in the earlier discussion. Figure 10 shows an inverse relationship between focused spot size and feature size, which may at first seem counterintuitive. Keeping in mind that the total energy contained in the laser pulse is held fixed, a smaller focused spot size provides higher energy flux directly to the center aperture of the PL. As a result, more energy comes out from the center aperture to enhance the temperature rise in the PCM layer, so the feature size becomes larger.

Next, a parametric study is performed for both operating parameters and PCM layer material properties. For the variables that are varied in the parametric study, Table 2 shows the base case values and the ranges over which they are varied. Operating parameters or material properties are varied one by one, keeping all other parameters fixed at their base case values, and the effect on feature size is shown. In discussing the results, it is useful to keep in mind that smaller feature radius and larger feature depth are often desired for the lithography process.

The effects of operating parameters on feature radius and depth are shown in Fig. 11. In this figure, the horizontal axis is the ratio of the operating parameter to its base case value. In some cases, the reciprocal of the operating parameter is used to make the feature radius plot (upper plot in Fig. 11) have positive slopes. This

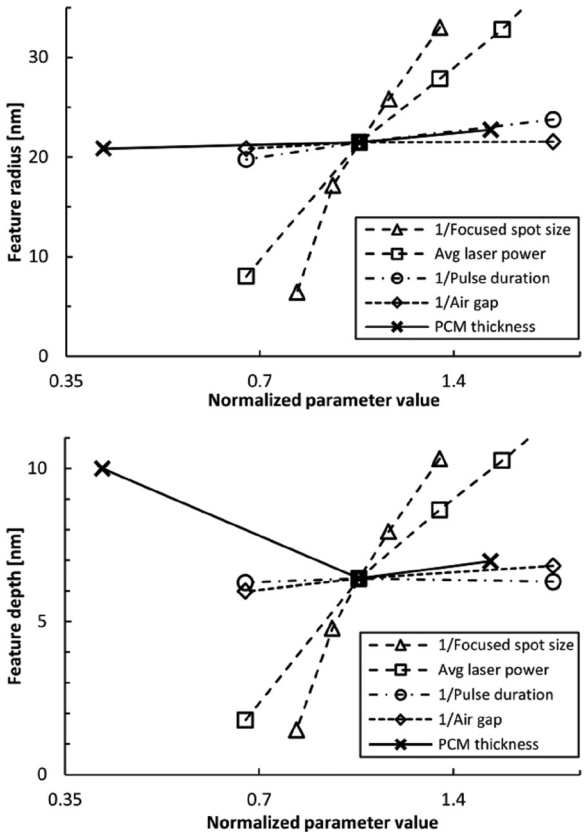

Fig. 11 Feature radius and depth as a function of operating parameter values (relative to base case)

makes it easier to compare the relative importance of parameters. As an example, laser pulse duration is one of the varied parameters for which the reciprocal is used, as indicated in the legend. Therefore, a value of 1.4 means that the laser pulse duration is 1.4 times *smaller* than the base case value. Note that feature radius increases with increasing laser power in accordance with the experimental trend shown in Fig. 4.

From inspection of Fig. 11, feature radius can be reduced for higher-resolution plasmonic lithography by reducing or increasing certain parameters but the feature depths are also reduced simultaneously for almost all the parameters. The one exception to this is the PCM layer thickness. A thinner PCM layer has a negligible effect on reducing the feature radius but dramatically increases the feature depth. Therefore, it may be possible to obtain *smaller* feature radius with the same feature depth. One possible approach is to reduce both average laser power and PCM layer thickness. As an example, by changing the PCM thickness and average laser power to become 40% and 79% of their typical values, respectively, the feature radius changes from the typical 22 nm to about

Table 2 Range of PCM properties and operating parameters included in parametric study—Values of PCM properties or operating parameters are varied one by one within the specified range from the base case

		Parametric study range	Base case value
PCM properties	PCM real refractive index	1.67–5.01	3.34
	PCM imaginary refractive index	1.67–5.01	2.93
	PCM thermal conductivity W/(m K)	0.84–1.4	1.12
	PCM volumetric heat capacity (MJ/(m^{3}K))	1.74–2.90	2.32
Operating parameters	Air Gap Thickness (nm)	1–3	2
	PCM Layer thickness (nm)	10–40	25
	Focused spot diameter (μm)	0.75–1.25	1
	Avg laser power reaching PL (mW)	3–25	4.5
	Laser pulse duration (ps)	6–18	12

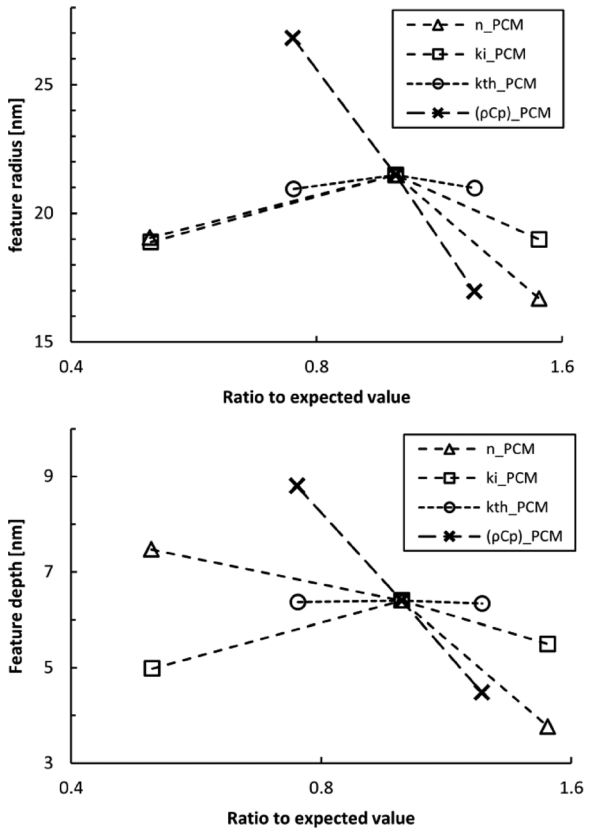

Fig. 12 Feature radius and depth as a function of PCM layer properties (relative to base case). In the legend, from top to bottom the PCM properties are the real and imaginary parts of the refractive index, thermal conductivity, and volumetric heat capacity.

15 nm with the feature depth unchanged. Physically, electromagnetic energy reflects at the bottom interface of the PCM layer. A thinner PCM layer absorbs less electromagnetic energy, allowing more electromagnetic energy to go through its thickness and reflect back to the PCM layer to be reabsorbed. Therefore, additional resistive heating takes place near the lower interface of the PCM layer to cause larger temperature rise at the bottom without significant effect on the region near the top surface.

Similarly, feature radius and depth are shown in Fig. 12 as functions of the PCM layer properties relative to their base case values. These results can be used either to account for the uncertainties in the assumed properties or to explore the effect of using a different material. From this figure, the volumetric heat capacity of the PCM layer, $(\rho C_p)_{PCM}$, has the largest effect on both feature radius and depth. Although volumetric heat capacity is not expected to vary dramatically for solids, it may still be worthwhile to determine the constituents and their percentages more accurately for the PCM layer instead of estimating them from the PCM sputtering target. As stated previously, the uncertainty of the PCM thermal conductivity only slightly affects feature radius and depth, because the thermal diffusion process takes much longer than the laser pulse duration. Observing the effect of the PCM refractive index, it appears that reducing the real part can lead to a smaller feature radius and larger feature depth. This suggests the possibility of improving the performance of plasmonic lithography by replacing the current TeO_x material with a different material having a smaller real part of the refractive index.

Conclusion

A model of the plasmonic lithography process has been developed that encompasses an electromagnetic wave model and a heat transfer model. Results from the numerical model confirm the strong electromagnetic energy focusing capability of the plasmonic lens with resolution in tens of nanometers as expected from the experimental result. Parametric studies for operating parameters and material properties are performed to optimize the lithography process and account for the uncertainties in material properties. Results are presented for the lithography feature radius and depth. These results suggest that the thickness of the phase-change material layer should be reduced for higher lithography resolution. Another option for higher resolution is to use a phase-change material with a smaller real part of the refractive index. Thus, the numerical model provides trends that suggest ways to optimize the plasmonic lithography process.

Acknowledgment

The authors would like to thank Shaomin Xiong for continuing the development of the plasmonic nanolithography system and making data available, Zhang Zhen for ellipsometry measurements, Jeongmin Kim for preparing samples for ellipsometry and 3-omega measurements, and Professor Laurent Pilon and Jin Fang for guidance and equipment for 3-omega measurements and data analysis. This work is financially supported by NSF Nano-scale Science and Engineering Center (NSEC) for Scalable and Integrated Nanomanufacturing (SINAM) (Grant No. CMMI-0751621).

Nomenclature

c_0 = speed of light in vacuum
C_p = specific heat
$\mathbf{E}$ = electric field phasor
$\mathbf{E_0}$ = constant electric field coefficient for Gaussian beam
$\mathbf{E_i}$ = incident electric field phasor
f_p = pulse frequency
g_p = Gaussian pulse function of time
$\mathbf{H}$ = magnetic field phasor
$\mathbf{J}$ = current density phasor
k = magnitude of wave vector
k_0 = magnitude of vacuum wave vector
k_i = imaginary part of the complex refractive index
k_{th} = thermal conductivity
$\mathbf{k}$ = unit vector in plane wave traveling direction
$\mathbf{k_{dir}}$ = directional wave vector
n = real part of the complex refractive index
n_c = complex refractive index
$\hat{\mathbf{n}}$ = surface unit normal vector
P_{ls} = time-average laser power arriving at plasmonic lens
Q = volumetric heat source
Q_{rh} = resistive heat loss
r = radius in cylindrical coordinates
r_0 = FWHM Gaussian pulse radius
$\mathbf{r}$ = position vector
$\mathbf{S_{av}}$ = time-average Poynting vector
$\mathbf{S_{av,i}}$ = incident time-average Poynting vector
t = time
t_0 = pulse time
T = temperature
w_0 = Gaussian beam waist
Δt = FWHM Gaussian pulse duration
ε_0 = vacuum permittivity
ε_r = relative permittivity
η = intrinsic impedance
ω = angular frequency
μ_0 = vacuum permeability
μ_r = relative permeability
ρ = density
σ = electrical conductivity
σ_t = standard deviation in time

Appendix A: Calculation of Incident UV Laser Electric Field Profile

The electric field profile of the UV laser inside the sapphire flying head is assumed to have a Gaussian spatial profile. By using cylindrical coordinates with $r^2 = x^2 + y^2$, the electric field profile of the positive z-propagating Gaussian beam is [18]

$$\mathbf{E_i}(r,z) = \mathbf{E_0}\frac{w_0}{w(z)}\exp\left(-\frac{r^2}{w^2(z)}\right)\cdot\exp\left[-j\left(kz+\frac{kr^2}{2R(z)}-\phi(z)\right)\right] \tag{A1}$$

where $\mathbf{E_0}$ is a constant electric field coefficient and w_0 is the beam waist

$$z_R = kw_0^2/2 \tag{A2}$$

$$w(z) = w_0\sqrt{1+(z/z_R)^2} \tag{A3}$$

$$R(z) = z\left[1+(z_R/z)^2\right] \tag{A4}$$

and

$$\phi(z) = \arctan(z/z_R) \tag{A5}$$

$\mathbf{E_0}$ is in the y-direction, which is the same as the electric field direction of the UV laser.

In order to use Eq. (A1) as incident electric field in one of the scattering boundaries, both $|\mathbf{E_0}|$ and w_0 must be calculated. Considering the focal plane of the Gaussian beam, which is located at $z = 0$, the field profile becomes

$$\mathbf{E_i}(r) = \mathbf{E_0}\exp\left[-r^2/w_0^2\right] \tag{A6}$$

Since the wavefront of the Gaussian beam is a flat surface at the focal plane, the magnetic field can be approximated by

$$\mathbf{H} = \frac{1}{\eta}\hat{\mathbf{k}}\times\mathbf{E} \tag{A7}$$

which is a relation between electric field and magnetic field for a plane wave [19]. In the above equation, $\hat{\mathbf{k}}$ is the unit vector in the plane wave traveling direction, which is the positive z-direction in this case. η is the intrinsic impedance, which is equal to

$$\eta = c_0\mu_0\mu_r/n_c \tag{A8}$$

where c_0 is speed of light in vacuum and μ_0 is vacuum permeability. The energy flux of the electromagnetic wave can be represented by the time-average Poynting vector, which is

$$\mathbf{S_{av}} = \frac{1}{2}\mathrm{Re}[\mathbf{E}\times\mathbf{H}^*] \tag{A9}$$

In the above equation, superscript "*" represents complex conjugate. Using the above equation and Eq. (A7), the magnitude of the Poynting vector of the incident laser can be written as

$$\left|\mathbf{S_{av,i}}\right| = \frac{n_c}{2c_0\mu_0\mu_r}|\mathbf{E_i}|^2 \tag{A10}$$

Moreover, by substituting Eq. (A6), Eq. (A10) becomes

$$\left|\mathbf{S_{av,i}}(r)\right| = \frac{n|\mathbf{E_0}|^2}{2c_0\mu_0\mu_r}\exp\left[-\frac{2r^2}{w_0^2}\right] \tag{A11}$$

For r_0 as a known FWHM focused radius of Gaussian beam, by inspecting Eq. (A11), w_0 can be solved from $1/2 = \exp(-2r_0^2/w_0^2)$, so

$$w_0 = r_0\sqrt{2/\ln 2} \tag{A12}$$

The continuous laser becomes a Gaussian pulse after passing through the optical modulator. The energy flux of a single laser pulse can be written as

$$\left|\mathbf{S_{av,i}}(r,t)\right| = \left|\mathbf{S_{av,i}}(r)\right|\cdot g_p(t) \tag{A13}$$

In the above equation, $g_p(t)$ is a Gaussian pulse function of time, and its expression is

$$g_p(t) = \frac{1}{\sigma_t\sqrt{2\pi}}\exp\left[-\frac{(t-t_0)^2}{2\sigma_t^2}\right] \tag{A14}$$

where σ_t is standard deviation in time and t_0 is pulse time. Similarly, for Δt as a known FWHM pulse duration, σ_t can be calculated from Δt as

$$\sigma_t = \Delta t/\left(2\sqrt{2\ln 2}\right) \tag{A15}$$

The amount of energy in each laser pulse can be related to the energy flux according to

$$\frac{P_{ls}}{f_p} = \int_{t=-\infty}^{\infty}\int_{r=0}^{\infty}\int_{\theta=0}^{2\pi}\left|\mathbf{S_{av,i}}(r,t)\right|\cdot r d\theta dr dt \tag{A16}$$

where P_{ls} is the time-average laser power arriving at the PL and f_p is pulse frequency. Both sides of Eq. (A16) are equal to the amount of energy in each laser pulse, and the resulting electric field coefficient is

$$|\mathbf{E_0}| = \sqrt{\frac{4c_0\mu P_{ls}}{f_p\pi n w_0^2 1[s]}} \tag{A17}$$

With Eqs. (A1), (A2)–(A5), (A12), and (A17), the incident electric field profile for the top scattering boundary in Fig. 7 is fully defined.

Appendix B: Calculation of Time-Dependent Heat Source

For evaluating the time-dependent heat source in the HT model, both time-independent resistive heating from the EMW model and Gaussian pulse function of time are used in the calculation. First, consider the steady harmonic resistive heating from the EMW model, which is

$$Q_{rh} = \langle\mathbf{J}\cdot\mathbf{E}\rangle \tag{B1}$$

In the above equation, $\mathbf{J}$ is current density phasor, and angle brackets, $\langle\ \rangle$, represent time average. By separating the real and imaginary parts, the complex refractive index is $n_c = n - jk_i$. With $\mathbf{J} = \sigma\mathbf{E}$ and Eq. (2), the steady harmonic resistive heating in Eq. (B1) can be written as

$$Q_{rh}(x,y,z) = \frac{nk_i\omega\varepsilon_0}{\mu_r}|\mathbf{E}|^2 \tag{B2}$$

By inspecting Eqs. (A10), (A13), and the above equation, the time dependency of the square of electric field magnitude is the same as that of the laser energy flux, and also the same as that of resistive heating. Therefore, the transient harmonic resistive heating is used as the transient heat source in the HT model, and its expression is

$$Q(x,y,z,t) = Q_{rh}(x,y,z)\cdot g_p(t) \tag{B3}$$

References

[1] Okazaki, S., 1991, "Resolution Limits of Optical Lithography," J. Vac. Sci. Technol. B, **9**(6), pp. 2829–2833.

[2] Marrian, C. R. K., Dobisz, E. A., Dagata, J. A., 1992, "Electron-Beam Lithography With the Scanning Tunneling Microscope," J. Vac. Sci. Technol. B, **10**(6), pp. 2877–2881.

[3] Melngailis, J., 1987, "Focused Ion-Beam Technology and Applications," J. Vac. Sci. Technol. B, **5**(2), pp. 469–495.

[4] Srituravanich, W., Pan, L., Wang, Y., Sun, C., Bogy, D. B., and Zhang, X., 2008, "Flying Plasmonic Lens in the Near Field for High-Speed Nanolithography," Nat. Nanotechnol., **3**(12), pp. 733–737.

[5] Pan, L., Park, Y., Xiong, Y., Ulin-Avila, E., Wang, Y., Zeng, L., Xiong, S., Rho, J., Sun, C., Bogy, D. B., and Zhang, X., 2011, "Maskless Plasmonic Lithography at 22 nm Resolution," Sci. Rep., **1**.

[6] Tompkins, H., and Irene, E. A., 2005, *Handbook of Ellipsometry*, William Andrew, Norwich, NY, Chap. 9.

[7] Yamane, T., Nagai, N., Katayama, S., and Todoki, M., 2002, "Measurement of Thermal Conductivity of Silicon Dioxide Thin Films Using a 3 Omega Method," J. Appl. Phys., **91**(12), pp. 9772–9776.

[8] Ito, E., Kawaguchi, Y., Tomiyama, M., Abe, S., and Ohno, E., 2005, "TeOx-Based Film for Heat-Mode Inorganic Photoresist Mastering," Jpn. J. Appl. Phys. Part 1, **44**(5B), pp. 3574–3577.

[9] Pan, L., 2010, "High-Throughput Plasmonic Nanolithography," Ph.D. thesis, University of California, Berkeley, Berkeley, CA.

[10] Cahill, D. G., and Pohl, R. O., 1988, "Lattice-Vibrations and Heat-Transport in Crystals and Glasses," Annu. Rev. Phys. Chem., **39**, pp. 93–121.

[11] Goodson, K. E., Flik, M. I., Su, L. T., and Antoniadis, D. A., 1994, "Prediction and Measurement of the Thermal-Conductivity of Amorphous Dielectric Layers," ASME J. Heat Transfer, **116**(2), pp. 317–324.

[12] COMSOL, 2012, *RF Module User's Guide*, Burlington, MA.

[13] Jin, J., 2002, *The Finite Element Method in Electromagnetics*, John Wiley & Sons, Inc., New York, Chap. 9.

[14] Touloukian, Y. S., 1970, *Specific Heat: Nonmetallic Solids* (*Thermophysical Properties of Matter*), Vol. 5, IFI/Plenum, New York.

[15] Touloukian, Y. S., 1970, *Specific Heat: Metallic Elements and Alloys* (*Thermophysical Properties of Matter*), Vol. 4, IFI/Plenum, New York.

[16] Walker, P., and Tarn, W. H., 1991, *CRC Handbook of Metal Etchants*, Taylor & Francis, Boca Raton, FL.

[17] Weaver, J., and Frederikse, H., 2001, "Optical Properties of Selected Elements," *CRC Handbook of Chemistry and Physics*, CRC Press, Boca Raton, FL, pp. 12–133.

[18] Siegman, A. E., 1986, *LASERS*, University Science Books, Sausalito, CA, Chap. 16.

[19] Ulaby, F. T., 2007, *Fundamentals of Applied Electromagnetics*, Pearson/Prentice Hall, Upper Saddle River, NJ, Chap. 7.